

Spatio-Temporal Control of THz Emission

Hsin-hui Huang

Academia Sinica

Saulius Juodkazis

Swinburne University of Technology <https://orcid.org/0000-0003-3897-2844>

Eugene Gamaly

Australian National University

Takeshi Nagashima

Tetsu Yonezawa

Koji Hatanaka (✉ kojihtnk@gate.sinica.edu.tw)

Academia Sinica

Article

Keywords:

Posted Date: March 22nd, 2022

DOI: <https://doi.org/10.21203/rs.3.rs-77877/v3>

License:   This work is licensed under a Creative Commons Attribution 4.0 International License.

[Read Full License](#)

Version of Record: A version of this preprint was published at Communications Physics on May 31st, 2022. See the published version at <https://doi.org/10.1038/s42005-022-00914-2>.

1 Spatio-temporal control of THz emission

2 **Abstract:** Polarization fine control of THz emission is demonstrated with a tilted micro-thin
3 water flow by the irradiation of two cross-linearly-polarized femtosecond laser pulses (800 nm,
4 35 fs, transform-limited) with spatio-temporal offsets. With an optimized horizontal offset
5 at $\sim 11 \mu\text{m}$ between the $\sim 8 \mu\text{m}$ focal spots and time delay at 4.7 ns, circularly-polarized
6 THz emission was obtained with its intensity enhancement more than 1,500-times if compared
7 with the single pulse irradiation. It is shown that the photon-number-based efficiency from
8 the laser to THz at 7.1×10^{-3} is achieved with the optimisation of the double pulse irradiation.
9 Polarization-resolved THz time-domain spectroscopy and time-resolved shadowgraphy imaging
10 revealed that the circularly-polarized THz emission originates from the focal volume in front of
11 the water flow. Coupling between a shockwave due to air-breakdown and water ablation-mediated
12 mass transport by the first pulse with a laser wake-field along the optical path of the main pulse is
13 responsible for the point-like single-cycle THz source.

14 1. Introduction

15 Intense THz wave sources are highly expected for further progresses in nonlinear THz science
16 and practical implementation of non-ionizing radiation in sensing and communications [1]. Solid
17 crystalline-based sources under laser irradiation have an inherent limitation due to the polarisation
18 and orientation sensitivity as well as due to material breakdown especially for intense laser
19 excitation for the developments of intense THz wave sources. On the other hand, an intense
20 laser irradiation to liquids is an emerging promising technique for THz emission [2–6]. It has a
21 possibility to tailor compositions of liquids and to explore conditions of different plasma densities
22 from under-dense (this study) to dense and different temperatures even for simultaneous hard
23 X-ray emission [7]. Especially appealing is the capability to refresh the irradiation spot on a liquid
24 flow/jet for a stable THz or X-ray emission source. It was empirically found that water-based THz
25 emission shows intensity enhancements up to 10^3 times when laser-pulse pairs with nanosecond
26 delay are applied [8]. This prompted a detailed experimental study of this phenomenon. Spectral
27 characterisation of light emission, light localisation and shock wave formation studied by imaging,
28 and polarisation-resolved time-domain spectroscopy (TDS) revealed detailed picture of the
29 light-matter interaction which realises a renewable pulsed (on demand) point-like THz source as
30 described in this study.

31 Here, a concept on fine-control of THz emission with the pre-pulse offsets under double pulse
32 excitation conditions is described (Fig.1). With nanosecond-temporal and micrometer-spatial
33 offsets of the pre-pulse irradiation under the double pulse excitation to a tilted water flow, THz
34 emission can be finely controlled in its intensity and polarization. This geometry verifies the
35 theoretically-predicted coupling in under-dense gaseous plasmas at $\sim 10^{17} \text{ W/cm}^2$ [9]. As one
36 possible hypothesis, we have discussed a mechanism on the basis of the transverse (t) plasma
37 density gradient $\nabla n_e^{(t)}$ (water ablation by the pre-pulse irradiation) which is coupled with the
38 longitudinal (l) electron velocity in the Langmuir plasma wave $\mathbf{v}_p^{(l)}$ (of the main pulse). This
39 mechanism generates circular electron current $[\nabla n_e^{(t)} \times \mathbf{v}_p^{(l)}]$, which induces circularly-polarised
40 THz emission.

41 2. Results

42 Experimental results of the imaging and spectral characterisation of the focal volume where the
43 laser pulse interaction with the water flow and ablated plume takes place is presented in the
44 dedicated sections. Polarisation analyses using TDS allowed us to reveal polarisation and to

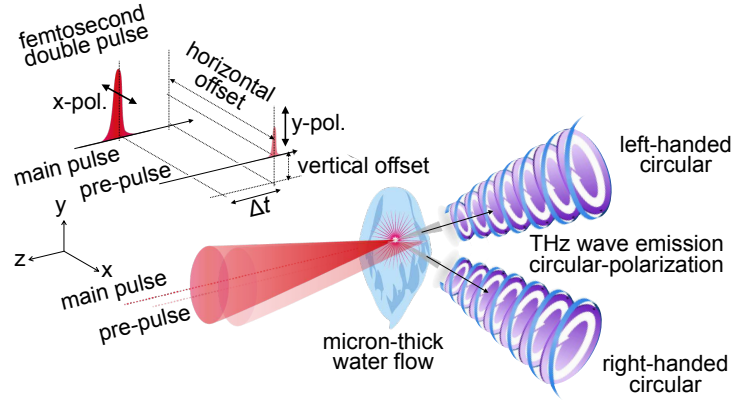


Fig. 1. A concept of THz emission control under the double pulse excitation with the pre-pulse spatio-temporal offsets and the tilted water flow. With such offsets, THz emission is finely controlled in its polarization from linear to circular with its handedness (helicity); left-handed circular (LHC, clock-wise when it is observed from the later time to the earlier time) and right-handed circular (RHC, counter-clock-wise) for the transmission and the reflection sides (or *vice versa*), respectively.

45 pinpoint the location of THz emission. Details of the experimental conditions are presented in
 46 Sec. 5.

47 2.1. Single pulse excitation of water flow

48 The polarization status of THz emission under the main pulse irradiation is shown in Fig.2(a). The
 49 polarization of the incident main pulse is horizontally-linear (x-pol. as usual, p-pol. to the water
 50 flow), circular, or vertically-linear (y-pol., s-pol. to the water flow). Though a circular-component
 51 is slightly observed when the main pulse is circularly-polarized, but even then, the resultant THz
 52 emission is dominantly horizontally-linearly polarized.

53 Time-integrated luminescence images under such irradiation condition are shown in Fig.2(b);
 54 blue emission components and a red spot are clearly observed. The component indicated by the
 55 light blue arrow is due to air-ionization at the tight laser focus since such emission is also observed
 56 even in air without the water flow. UV-visible emission spectroscopy also confirmed emission
 57 peaks of atoms and ions such as oxygen or nitrogen [10] at different ionisation states. Another
 58 blue component indicated by the dark blue arrow is due to laser ablation, ejection of ionised water
 59 into ablation plume from the water flow. This component is always vertical to the water flow with
 60 different laser incident angles as shown in Fig. S1 (in Supplement). Distinguished line emission
 61 from hydrogen shown in Fig.2(c) is a signature of water breakdown. The red spot is at the tight
 62 laser focus due to laser-plasma on the flow surface; the effective laser focus size on the water flow
 63 can be estimated from this image to be $8\mu\text{m}$ at largest. The emission spectrum shown in Fig.2(c)
 64 indicates that the incident main pulse is blue-shifted due to self-phase modulation (SPM) by the
 65 self-generating plasma [11, 12], which is usual in the case of hard X-ray emission from a water
 66 flow [13]. This blue-shift is an indication of the laser-plasma coupling, which is essential feature
 67 at the used $1 - 10 \text{ PW/cm}^2$ intensities. The temporal frequency shift $\omega(t) = \omega_0 + \alpha_S t$ due to
 68 SPM is defined by the nonlinear refractive index of the medium n_2 , interaction length L , and the
 69 laser pulse intensity I_l and duration t_p as $\alpha_S = \frac{4\pi L n_2 I_l}{\lambda_l^2}$. For typical values in this experiment
 70 $L = 100 \mu\text{m}$, $t_p = 40 \text{ fs}$, $I_l = 10 \text{ PW/cm}^2$ and $\Delta\omega_0/\omega_0 = 10\%$ ($\Delta\lambda = 80 \text{ nm}$), the effective value
 71 of $n_2 = 60 \times 10^{-20} \text{ cm}^2/\text{W}$ in the region of the pre-pulse-induced plume, which is almost an
 72 order of magnitude larger than the typical $n_2 = 8 \times 10^{-20} \text{ cm}^2/\text{W}$ of air at 800 nm [11, 12] (see

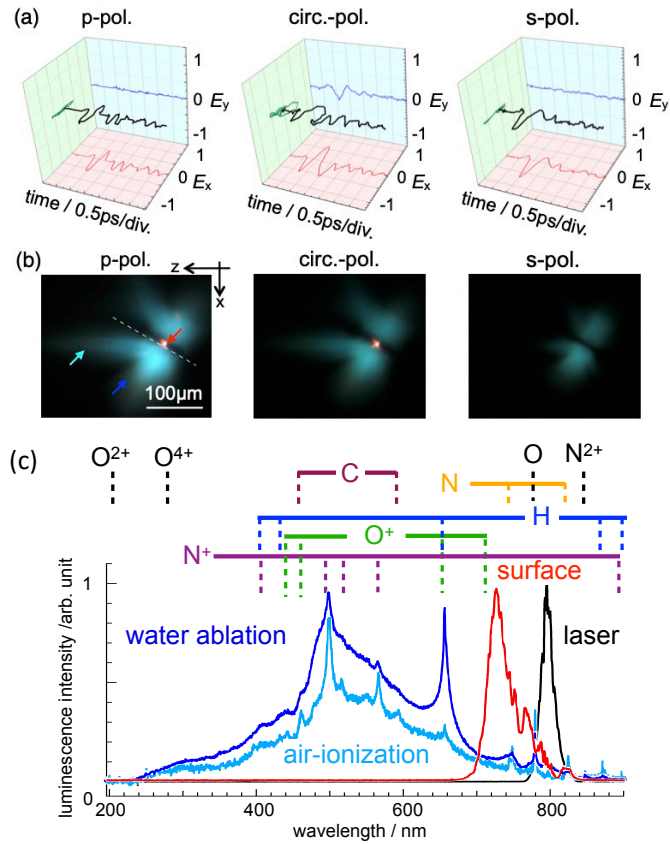


Fig. 2. (a) TDS signals (for the transmission side) measured with THz polarizers (wire-grids) under the single pulse excitation (0.4 mJ/pulse, 35 fs, 800 nm, 0.5 kHz, the laser incident angle to the normal of the flow is at 60° .) with different polarization of horizontally-linear (x-pol. as usual, p-pol. to the water flow), circular, or vertically-linear (y-pol., s-pol. to the water flow). (b) Time-integrated luminescence images observed from the top only with the main pulse irradiation. The white dotted line represents the flow surface and the black area behind the dotted line is the thickness of the flow $\sim 17 \pm 3 \mu\text{m}$. The laser irradiates the water flow from the left to the right in the image. The emission indicated by the light blue arrow is due to air ionization. The spot indicated by the red arrow represents the tight focus of the incident laser on the flow surface; the effective laser focus size on the water flow can be estimated to be $8 \mu\text{m}$ at largest. The other component going diagonally downward indicated by the dark blue arrow is considered to be due to laser ablation of the water flow. Other blue emission in the top-right is reflection from the flow surface. (c) Time-integrated luminescence spectra at the positions indicated by the arrow in (b) and the laser emission spectrum (in black). Sharp emission lines observed in air-ionization can be assigned to be from ions of oxygen, nitrogen, and argon [10]. The blue-shift of the emission from the focal spot is due to self-phase modulation of laser pulse. Spectral region at wavelengths shorter than $\sim 320 \text{ nm}$ has lower sensitivity due to reduced transmission of a signal collection optics.

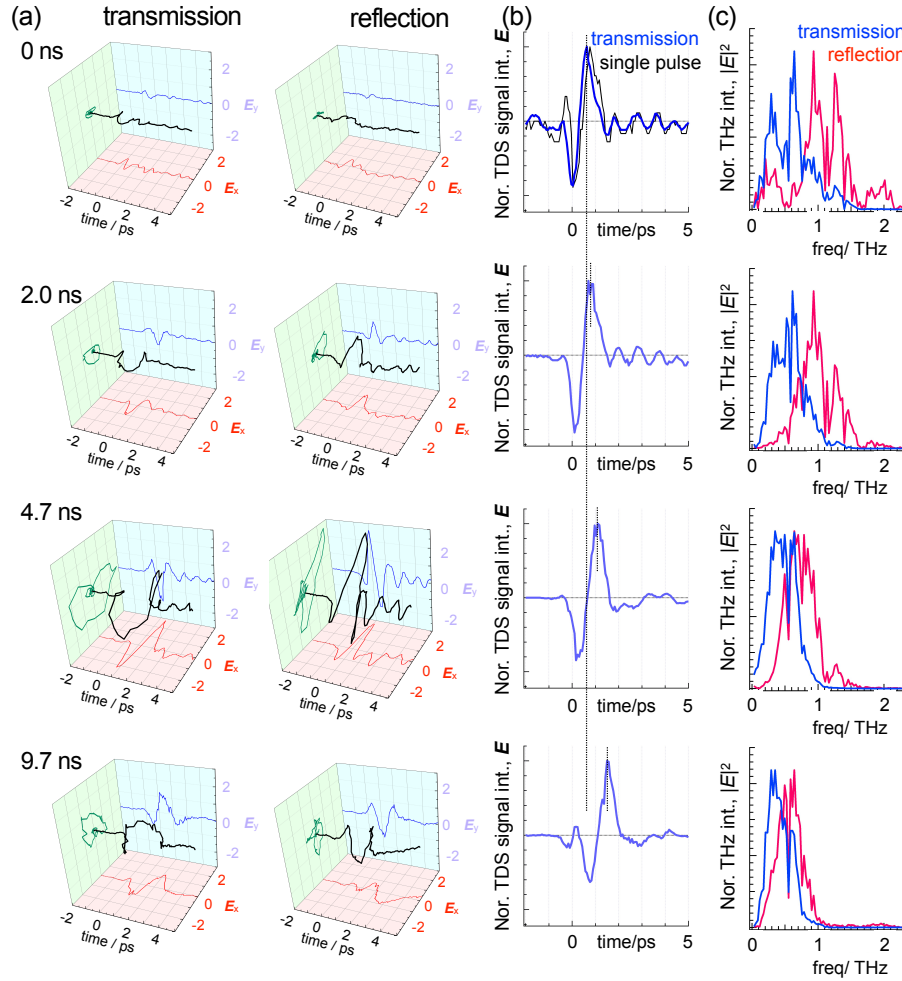


Fig. 3. (a) TDS signals for the transmission and the reflection sides measured at different delay times with the wire-grids under the double pulse excitation with the pre-pulse (y-pol.) at 0.2 mJ/pulse and the main pulse (x-pol.) at 0.4 mJ/pulse. The pre-pulse spatial offset is fixed at $(\Delta x, \Delta y) = (11 \mu\text{m}, 0 \mu\text{m})$. THz polarization changes from linear in the single pulse excitation as shown in Fig.2(a) to circular. (b) TDS signals measured without the wire-grids under the double pulse excitation in the transmission side (normalized). As the delay time between the two pulses increases, the signal peak delays. The similar tendency of the peak shift is also observed for the reflection side. (c) THz emission spectra obtained from discrete Fourier transform of TDS signals (normalized). As the delay time increases, the emission spectra shifted towards the lower frequency (red-shift in wavelength).

74 2.2. Double pulse excitation: dependence on the delay time

75 Under the double pulse excitation condition with the fixed spatial offset for the pre-pulse at
 76 $(\Delta x, \Delta y) = (11 \mu\text{m}, 0 \mu\text{m})$, the results apparently change as shown in Fig.3(a); as the delay time
 77 between the two pulses increases, the polarization status of THz emission dynamically changes
 78 to circular-polarization from horizontally-linear under the single pulse excitation as shown in
 79 Fig.2(a). As a representative data set, THz polarization when the delay time is at 4.7 ns is

80 left-handed circular (LHC, clock-wise when it is observed from the later time to the earlier time)
81 and right-handed circular (RHC, counter-clock-wise) for the transmission and the reflection
82 sides, respectively. Furthermore, with the spatio-temporal offsets $(\Delta x, \Delta y, \Delta t) = (11 \mu\text{m}, 0 \mu\text{m},$
83 $4.7 \text{ ns})$, THz emission intensity increases 1,500-times higher than in the single pulse irradiation
84 as $|E|^2$ -intensity in DFT spectra over the 0-3 THz region [8]. Considering the report on the energy
85 conversion efficiency from 800nm to THz wave with a ZnTe<110> crystal at 1.25×10^{-5} [14], the
86 photon-number-based conversion efficiency under the double pulse irradiation can be estimated
87 7.1×10^{-3} .

88 As shown in Fig.3(b), close look-up of the TDS signal wave-forms shows their peak delay
89 as the delay time increases. Furthermore, THz emission spectra obtained as discrete Fourier
90 transform of TDS signals generally show their peak shift toward the shorter frequency as shown
91 in Fig.3(c); more precisely the shift is larger in the transmission side than in the reflection side.

92 Fig.4(a) shows time-integrated luminescence images at different delay times only with air
93 (without the water flow). The pre-pulse spatial offset is fixed at $(\Delta x, \Delta y) = (11 \mu\text{m}, 0 \mu\text{m})$. In
94 the case only with air, though a stretched rugby ball-like blue emission is observed at the focus
95 under the single pulse excitation, the spatial distribution of the blue emission, which reflects the
96 intensity spatial distribution of the incident main pulse, shows distorted shapes under the double
97 pulse with the pre-pulse irradiation with the spatial offset. As the delay time increases, the spatial
98 distribution changes. This is due to the shockwave expansion from the volume of air-ionization
99 due to the pre-pulse irradiation. The expansion velocity of the shockwave front is estimated to be
100 about 7 km/s initially at $\Delta t = 2.0 \text{ ns}$ and it slows down to about 1 km/s at $\Delta t = 14.7 \text{ ns}$ as shown in
101 Fig. S2 (in Supplement).

102 Under the double pulse excitation with the water flow shown in the time-resolved shadowgraphy
103 Fig.4(b) and the luminescence images Fig.4(c), another shockwave formation due to laser ablation
104 by the pre-pulse excitation to the water flow (therefore this shockwave front carries ablation
105 plume of ionised/atomised water), its expansion in front of the flow, and formation of cavitation
106 bubbles in the flow are clearly observed. In the shadowgraphy, a white dotted line and black
107 dotted lines represent the focus of the incident main pulse on the flow surface and the expanding
108 shockwave front, respectively. The expansion velocity of the shockwave front is estimated to be
109 about 8-10 km/s initially at $\Delta t = 2.0 \text{ ns}$. In the luminescence image, the positions indicated by the
110 arrows in orange and red match the shockwave front and the focus of the incident main pulse on
111 the flow surface in the shadowgraphy, respectively. Fig.4(d) shows the emission spectra for the
112 shockwave front (orange) and the flow surface (red) with the peak wavelength at 720 nm and
113 770 nm, respectively. These spectral shifts are due to the self-phase modulation-based blue-shift
114 from the original laser pulse at 800 nm as discussed in the previous section. The results obtained
115 indicate that the main pulse interacts with the shockwave front under this double pulse excitation
116 condition and injects ablation plume/plasma, which is driving a wake-field at incident intensity
117 of $\sim 10^{16} \text{ W/cm}^2$. Even in the double pulse irradiation in air, luminescent halo is formed when
118 ionised air is pushed from the side into the main-pulse [15]. This injection from the side is an
119 important aspect of THz emission from sub-wavelength focal region of $\sim 100 \mu\text{m}$ length.

120 2.3. Double pulse excitation: dependence on the pre-pulse spatial offset

121 Experiments were extended to reveal the effects of spatial offsets between the two pulses for
122 control of THz emission. Fig.5 shows the results of TDS measurements with the wire-grids
123 for the transmission (a) and the reflection (b) sides. The delay time between the two pulses is
124 fixed at 4.7 ns. In the transmission side, as the horizontal offset becomes large along the x-axis
125 from the condition in Fig.3 (a) at $(\Delta x, \Delta y) = (11 \mu\text{m}, 0 \mu\text{m})$, THz polarization changes from
126 elliptical to horizontally-linear. As the vertical offset with the fixed horizontal offset at $\Delta x =$
127 $11 \mu\text{m}$, THz polarization changes to horizontally-linear and back to circular but with opposite
128 handedness, left-handed (LHC, in blue) to right-handed (RHC, in red). Interestingly, an apparent

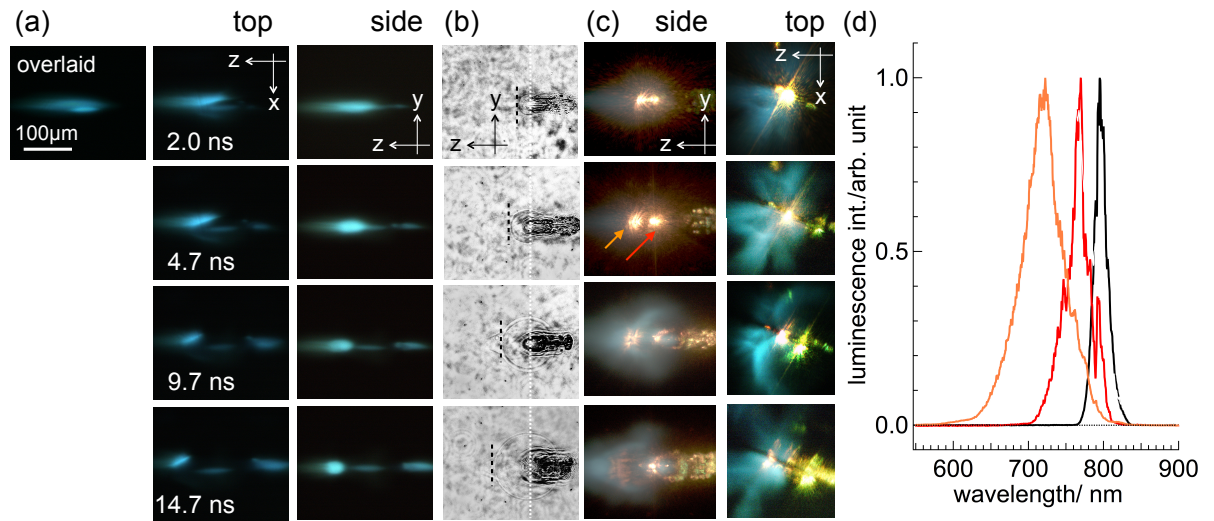


Fig. 4. Imagies of micro-explosion when the pre-pulse spatial offset is fixed at $(\Delta x, \Delta y) = (11 \mu\text{m}, 0 \mu\text{m})$. (a) Time-integrated luminescence images at different delay times only in air (without the water flow). (b) Time-resolved shadowgraphy with the water flow from the side with picosecond white light back-illumination. The short dotted line in black represents the shockwave front. (c) Time-integrated luminescence images in different delay times with the water flow. The arrows in orange and red in the luminescence image indicate the light emission at the shockwave front and the laser focus on the flow surface, respectively. The luminescence spectra from these positions are as shown in (d) with the laser emission spectrum centered at 800 nm.

129 THz intensity enhancement nor THz circular-polarization were not observed when the pre-pulse
 130 irradiates the water flow with the horizontal offset with negative values. On the other hand in the
 131 case only with air without the water flow, as shown in Fig. S3 (in Supplement), the tendency
 132 of the THz polarization dependent on the pre-pulse spatial offset is homogeneous in its radial
 133 direction (as expected from its symmetry). This indicates that the asymmetric characteristic of
 134 the tilted water flow is important.

135 In the reflection side as shown in Fig.5 (b), distorted THz polarization is clearly observed.
 136 Similar to the case in the transmission, THz intensity enhancement or THz circular-polarization
 137 is not observed when the pre-pulse irradiates with the horizontal offset at negative values (the
 138 pre-pulse irradiates the water flow before its focus). Another characteristic observed is that the
 139 handedness (helicity) of the circular-polarization is always opposite to that in the transmission;
 140 when the polarization is left handed-circular (LHC) in the transmission, it is right handed-circular
 141 (RHC) in the reflection and *vice versa*. Furthermore, another tendency observed clearly is that
 142 the distortion of the polarization especially along the vertical offset with the fixed horizontal
 143 offset at $\Delta x = 11 \mu\text{m}$ shows a radial characteristic of polarisation.

144 Fig.6 shows (a) time-integrated luminescence images in air without the water flow with different
 145 pre-pulse horizontal offsets with the fixed vertical offset at $0 \mu\text{m}$, (b) time-resolved shadowgraphy
 146 under the pre-pulse excitation without the main pulse, and (c) time-integrated luminescence
 147 images with the water flow under the double pulse excitation. The delay time between the main
 148 pulse is fixed at 4.7 ns. Similar to the images shown in Fig.4 (a), the intensity spatial profile of
 149 the incident main pulse is distorted but it is dependent on the pre-pulse horizontal offset. The
 150 pre-pulse irradiation position on the water flow also changes with the offset as shown in Fig.6
 151 (b) since the water flow is 60° -tilted to the laser irradiation axis. As described previously, a

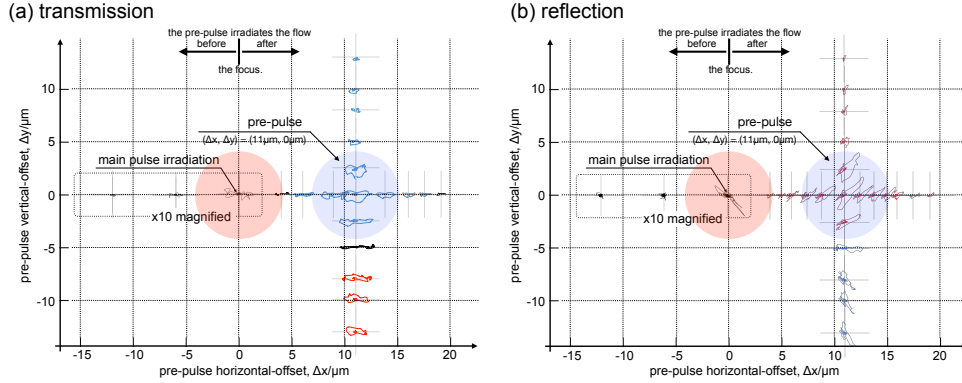


Fig. 5. Projections of TDS signals measured with wire-grids to x-y plane (as the plot on the green panel in Fig.2(a) or Fig.3(a)) under the double pulse excitation with the delay time at 4.7 ns. The plots in blue and red represent left-handed circular (LHC) and right-handed circular (RHC), respectively. The plots in black represent almost linearly-polarized emission. The red circle in each plot represents the effective area ($8 \mu\text{m}$ in diameter) of the main pulse irradiation.

152 shockwave expansion due to the air-ionization induced by the pre-pulse irradiation is observed as
 153 shown in the inset of Fig.6, which is indicated by the black arrows. Such shockwave due to the
 154 air-ionization is still observed when the horizontal offset is $11 \mu\text{m}$, while such shockwave is not
 155 observed when the horizontal offset is $-19 \mu\text{m}$. This is considered to be due to the 60° -tilted
 156 water flow; the pre-pulse irradiates the water flow after or before the focus in air when the offset
 157 is at $11 \mu\text{m}$ or $-19 \mu\text{m}$, respectively. In luminescence images shown in Fig.6 (c), orange emission
 158 is observed when the pre-pulse offset is even at $-19 \mu\text{m}$ as well as at $11 \mu\text{m}$. However, in the case
 159 with the offset at $-19 \mu\text{m}$, the emission is from the shockwave from the water surface due to laser
 160 ablation and its structure can be different from the structure when the offset is at $11 \mu\text{m}$. The
 161 details will be discussed later in the Discussion section with Fig. 9.

162 3. Discussion

163 A charge current or redistribution on ~ 1 ps time scale will generate ~ 1 THz emission.
 164 Polarisation of detected signal depends on the current direction and the position of detectors.
 165 Linearly-oscillating current will generate toroidal pattern of E -field. Depending on the position
 166 of detector, polarisation can be undefined (on the axis of oscillating dipole along which
 167 there is no dipole emission) or linear (perpendicular view to the oscillating linear current).
 168 Circularly-oscillating/redistributing charges will emit circularly-polarised E -field when observed
 169 perpendicular to the current loop.

170 As observed in THz emission from gas jets in vacuum, radial (linear) polarisation was observed
 171 and was defined with orientation of concentration gradient of expanding ion-clouds [16]. Our
 172 group also observed recently such THz emission dependent on the density gradient at the
 173 shockwave front in air even at atmospheric pressure under the same experimental condition as
 174 in this paper [15]. The gradient of injected material (ablation plume and ionised air) into the
 175 path of the main-pulse observed in the experiments is important for further discussion. The
 176 pre-pulse irradiation creates such plasma/gas gradients which are injected into the optical path of
 177 the main-pulse from side at different time moments. Apparently, optimisation of space and time
 178 of such injection defines efficiency and polarisation of THz emission.

179 The irradiated spot on the water flow was close to the geometrical focus of diameter $2w_0 =$
 180 $2 \times 0.61\lambda_l/NA \approx 8 \mu\text{m}$ as determined by direct imaging; $NA = 0.125$ is the effective numerical

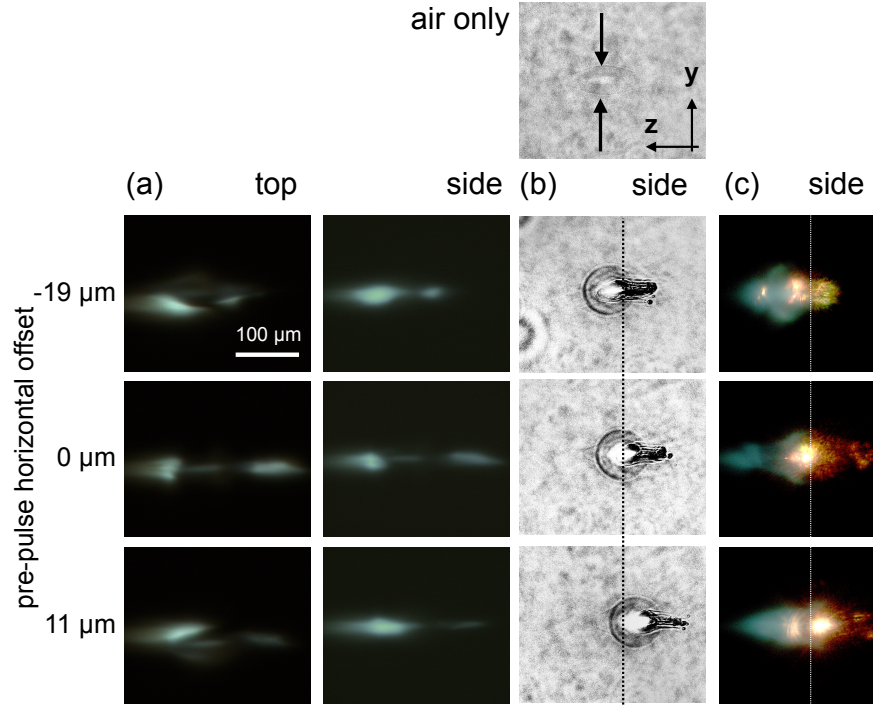


Fig. 6. (a) Time-integrated luminescence images in air without the water flow when the pre-pulse horizontal offset is at $-19 \mu\text{m}$, $0 \mu\text{m}$, or $11 \mu\text{m}$ with the fixed vertical offset at $0 \mu\text{m}$. The delay time between the main pulse is fixed at 4.7 ns . (b) Time-resolved shadowgraphy with picosecond white-light back-illumination under the pre-pulse excitation without the main pulse. The arrows indicate the shockwave front due to the air-ionization induced by the pre-pulse irradiation. (c) Time-integrated luminescence images with the water flow under the double pulse excitation from the side. The inset on the top is a time-resolved shadowgraphy in air without the water flow only with the pre-pulse irradiation. The arrows indicate the shockwave front due to the air-ionization induced by the pre-pulse irradiation.

181 aperture of the off-axis parabolic mirror. The axial extent of the focal region, the depth of
 182 focus $2z_R = 2n\pi w_0^2/\lambda \approx 120 \mu\text{m}$ exactly what was observed in experiment. Under such
 183 focusing conditions, there was no considerable change of the light-matter interaction volume
 184 due to self-focusing, which is typically used in THz emission in air (see Supplement S1.3 for
 185 the estimates of ablation conditions). Hence, THz emission is induced from the volume of
 186 sub-wavelength (for THz wave) cross sections and constitutes a point-like emitter which is useful
 187 for THz optical applications. In the following sections, we present a mechanism discussion
 188 as one possible hypothesis on how circularly-polarized THz emission, cyclotron-like electron
 189 trajectories in other words, is induced under the double pulse excitation.

190 3.1. Single pulse excitation

191 The laser irradiation conditions are in the range of $6\text{-}26 \text{ PW/cm}^2$ with ponderomotive field action
 192 and wake-field formation far from the relativistic conditions defined by the ratio of electron
 193 quiver velocity to the speed of light $a_0 \equiv v_q/c \approx 0.14$ for the highest intensity. The plasma under
 194 consideration is underdense $\omega > \omega_c$ for the used laser wavelength $\lambda = 800 \text{ nm}$, where ω_c is the
 195 critical density and $\omega = 2\pi c/\lambda$. At the used intensities, ionisation of air takes place at the waist

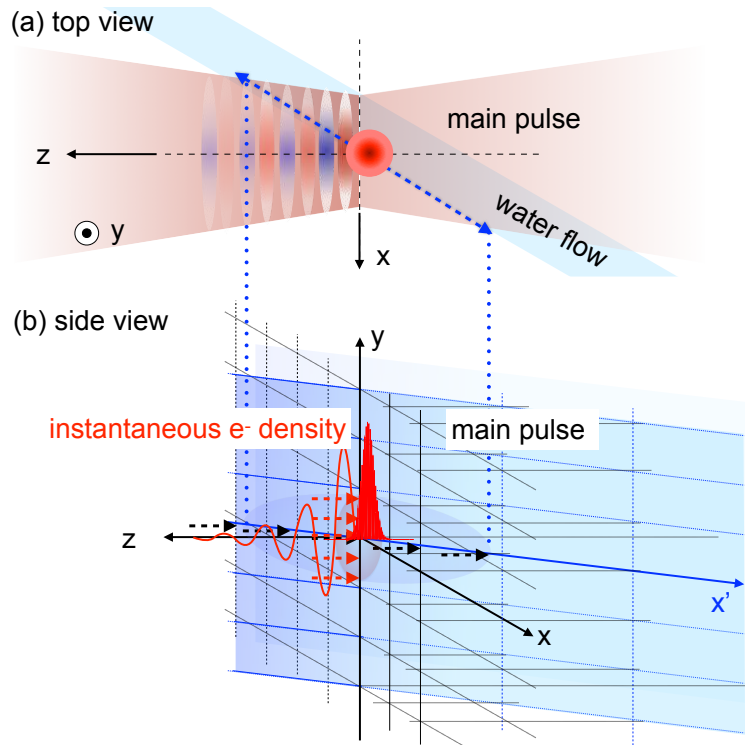


Fig. 7. Geometry of the wake-field formation under the single pulse excitation with the incident angle at 60° to the water flow.

196 of the beam even without the water flow. Self-action of instantaneous ionisation and propagation
 197 of laser pulse creates a coupled plasma-light system, the wake-field. The ponderomotive force
 198 which for electron is $F_p = -\frac{e^2}{4m_e\omega^2}\nabla I$, where I is the laser intensity forming the wake structure,
 199 a longitudinal plasma wave.

200 A circular focal diameter of the laser focus projects onto the water flow as an ellipsis which is
 201 twice-wider elongated since $\cos(60^\circ) = 0.5$ as compared with its extension along y-axis. This
 202 corresponds to the moving ionisation pattern on the water flow surface schematically shown in
 203 Fig. 7(a). After the laser pulse ionisation, the charge relaxation is expected to occur along the
 204 direction of the initial surface of water flow. Hence, the strongest current component is expected
 205 to be along x-axis. This determines the polarisation of THz emission. Regardless the polarisation
 206 of the incident pulse, THz wave was E_x -polarised. Even when the incident polarisation was
 207 circular, the THz emission was only slightly elliptical with prevailing linear component as for
 208 any other irradiation with the linear polarisation.

209 3.2. Double pulse excitation: the delay time effect

210 In the experiments with different delay times, TDS signal peak delays (Fig.3 (b)) and spectra
 211 shifts of THz emission toward the shorter frequency (Fig.3 (c)) are clearly shown. Furthermore,
 212 the positions of the expanding shockwave front in the shadowgraphy match the positions of the
 213 light emission observed in luminescence images (Fig.4 (b) and (c)). This tendency, with the
 214 emission spectrum of the shockwave front shown in Fig.4 (d), indicates that the THz emission
 215 under the double pulse excitation is mainly from the shockwave front. Fig.8 (a) shows the TDS
 216 peak delay as the function of the delay time and the distance estimated from the TDS peak

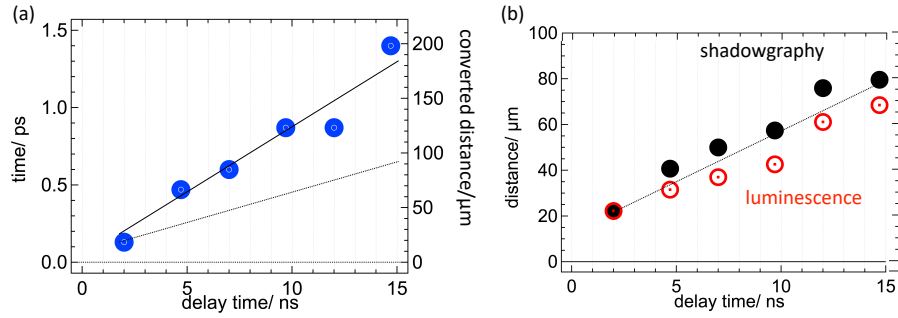


Fig. 8. (a) TDS peak delay (shown in Fig.3 (b)) as a function of the delay time. The TDS peak delay is converted to the distance under the assumption that the THz emission in front of the water flow experiences the passage through water considering that the refractive index of water at 1-THz is 2.12 [17]. The solid line is an eye guide and the dotted line is a converted distance under the assumption that the THz emission passes through water but with the density at 0.5. (b) The distance of the shockwave expansion (a) shown in Fig.4 (b) and (c).

217 delay under the assumption that the THz emission passes through additional volume with water
 218 component due to laser ablation from the water flow. If the volume is with a half density of water,
 219 the slope shown as a dotted line in Fig.8 (a) match the shockwave expansion dynamics observed
 220 in the imaging experiments shown in Fig.8 (b). This data analysis indicates that the THz emission
 221 under the double pulse excitation is induced mainly at the front of the expanding shockwave, the
 222 upstream side far from the flow surface which is the case of the single pulse excitation.

223 3.3. Double pulse excitation: pre-pulse spatial offset

224 One apparent result shown in Fig.5, is that THz intensity enhancements and the polarisation
 225 change are induced only when the pre-pulse spatial offset along x-axis is positive. The results
 226 shown in Fig.6 indicate that the shockwave due to the air-ionization, which has been also observed
 227 and results in linearly-polarized THz emission in air under the same double pulse excitation [15],
 228 plays a key role for such characteristic changes under the double pulse excitation. Air breakdown
 229 by the pre-pulse pushes ionised air into the optical path of the main pulse and the condition is
 230 very different for the $+x$ and $-x$ positions. Based on the results described, Fig.9 shows schematic
 231 diagrams of the configurations in front of the water flow from the top for the cases $\Delta x = -19 \mu\text{m}$
 232 (a) and $+11 \mu\text{m}$ (b). When the offset is at $\Delta x = -19 \mu\text{m}$, the pre-pulse irradiates the water flow
 233 before the focus and a shockwave material transport into the optical path of the main pulse is not
 234 efficient (a weaker ablation of water and not synchronised with the wake-field). When the offset
 235 is at $\Delta x = +11 \mu\text{m}$, the pre-pulse irradiates the water flow after it focuses tightly in air. This is
 236 because the water flow is tilted at 60° . Apparently, such interference between the shockwaves due
 237 to the air-ionization and the water ablation is observed clearly when the pre-pulse horizontal offset
 238 is at $\Delta x = +11 \mu\text{m}$ as shown in Fig.9(d), while such shockwave formation due to air-ionization is
 239 not observed at all when the pre-pulse horizontal offset is at $\Delta x = -19 \mu\text{m}$ as shown in Fig.9(c).

240 Water ablated by the pre-pulse irradiation is expanding and entering into the optical path of the
 241 main-pulse. A more dense region formed by the pre-pulse at the focal breakdown in air facilitates
 242 the formation of the wake-field as the main pulse propagates into the matter/plasma driven by the
 243 shockwave from the water ablation by the pre-pulse. The wake-field is schematically shown in
 244 Fig. 7, which pushes electrons with the advancing front at velocity \mathbf{v}_p . If the pre-pulse-induced
 245 plume is pushed into the right location (the space and time synchronisation is essential), there
 246 will be an effective coupling of the wake-field velocity \mathbf{v}_p and the perpendicular electron density

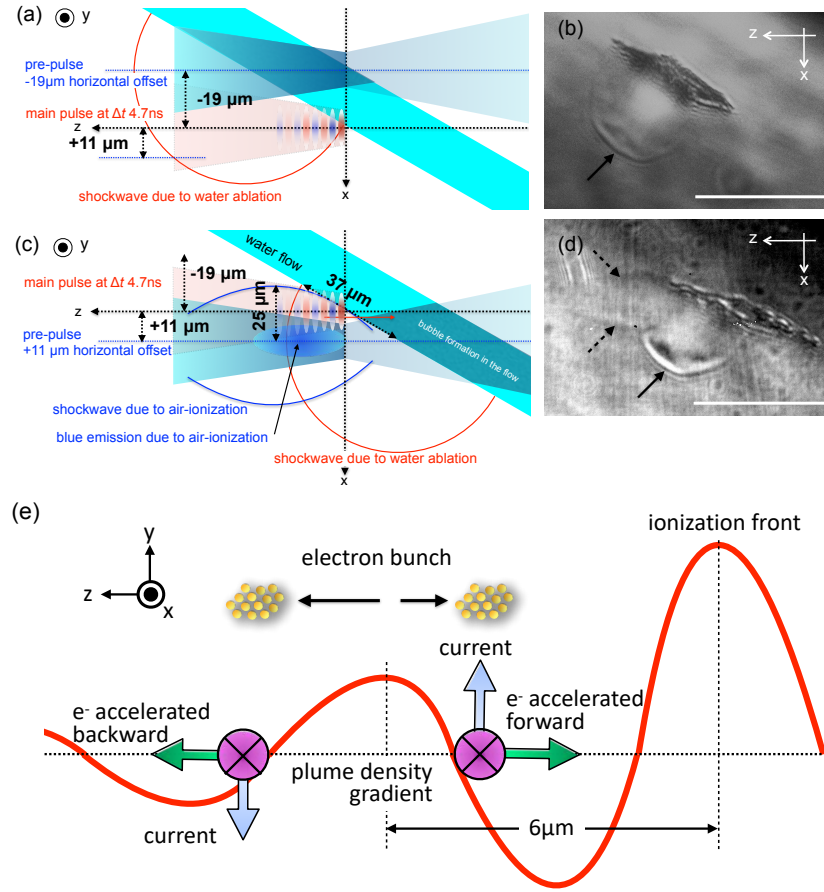


Fig. 9. Schematics of the water flow under the double pulse excitation with the delay time at 4.7 ns from the top with the pre-pulse horizontal offset at (a) -19 μm and (c) 11 μm. Time-resolved shadowgraphy of the water flow from the top only with the pre-pulse excitation (the horizontal offset at (b) -19 μm and (d) 11 μm). The arrows in solid and dotted lines represent the shockwave front due to the water flow ablation and the air-ionization (observed only for the horizontal offset at 11 μm), respectively. The scale bars in the shadowgraphy images correspond to 100 μm. (e) A hypothetical schematic model of the wake-field (side-view) formed by the main pulse interaction with the pre-pulse-induced ablation plume. Coupling of wave field and charge gradient $[\nabla n_e^{(r)} \times \mathbf{v}_p^{(l)}]$, defines the handedness of circular current, hence, polarisation of emitted THz, depends on the position/timing of the side injection.

247 gradient ∇n_e (see details in Supplement S1.3)). However, if the injection of the pre-pulse-induced
 248 plume is arriving a half period of the wake-field later (Fig. 7(b)), electrons will be pushed back
 249 (an opposite direction of the wave-field-induced electron transport). It was predicted theoretically
 250 that circularly-polarised THz emission will result from such coupling $\nabla n_e \times \mathbf{v}_p$ [9, 18, 19] and
 251 the polarization handedness depends on the sign of the cross-product. Change of the sign of
 252 \mathbf{v}_p depends on the geometrical location of the pre-pulse and the geometrical structure of the
 253 wake-field. Apparently, the expanding plume which entered the optical path of the main pulse
 254 from the above caused the RHC THz emission and from the below caused the LHC THz emission
 255 (this is consistent with the side view structure of the wake-field shown in Fig. 7(b)). The factors

256 which breaks the top-bottom (vertical) symmetry along y-axis are combined due to the water
257 flow and the gravity acting on an aerosol formed by the low repetition 0.5 kHz laser pulses in the
258 experiment. The plume due to water ablation is charge-coupled and composed of very different
259 masses: electrons, protons, and ionised oxygen atoms.

260 The period of the wake-field $\lambda_{pe} = 2\pi/k_{pe} \approx 5.9 \mu\text{m}$ (in time $2\pi/\omega_{pe} = 20 \text{ fs}$) is defined by
261 the Langmuir frequency $\omega_{pe} = \sqrt{n_e e^2 / (\epsilon_0 m_e)}$ and the skin depth $k_{pe} = \omega_{pe}/c \approx 0.9 \mu\text{m}$ for the
262 plasma density which is by 30% higher than the molecular air density $n_e = 1.3 \times [2.5 \times 10^{19}] \text{ cm}^{-3}$
263 (as seen by the main pulse); then the group velocity $v_g = c^2 k / \omega = c\sqrt{\epsilon} = 0.99c$. The maximum
264 of THz emission was observed at $\Delta x = 11 \mu\text{m}$ offset under the optimised ($\Delta t = 4.7 \text{ ns}$) double
265 pulse exposure with the diameter of the focal spot at $\sim 8 \mu\text{m}$. Maximising the plasma density
266 gradient $\nabla n_e^{(t)}$ (transverse) coupling with electron velocity $v_e^{(l)}$ (longitudinal) is required for the
267 generation of the circular current [9]. Formation of the electron density gradient ∇n_e (transverse)
268 facilitates induction of a rotational current $\nabla \times \mathbf{j} = e \nabla n_e \times \mathbf{v} \neq 0$, where \mathbf{v} is the longitudinal
269 electron velocity in the wake, hence, $\nabla \times \mathbf{v} \equiv 0$ [18] (see [Supplement S1.3](#) and [Fig. 9](#)).

270 THz wave emission in the reflection and transmission directions in respect to the water flow
271 has similar intensities but opposite polarisation handedness. The highest intensity of THz wave
272 emission from the water flow under the double pulse excitation in $|\mathbf{E}|^2$ (as photon numbers)
273 is about 1 GW/cm^2 based on the THz wave emission from the ZnTe crystal at the saturation
274 regime [20]. For the incident laser power of $\sim 1 \text{ PW/cm}^2$, the conversion efficiency from the
275 near-IR laser to THz wave in this study is estimated to be 10^{-6} . Further enhancements are
276 expected in other liquids such as gold nano-colloidal aqueous suspensions as reported in hard
277 X-ray emission [21].

278 4. Conclusion and Outlook

279 A simple two-laser pulse irradiation with micro-meter spatial offsets and nanosecond time delay
280 to a micro-thin water flow is shown to generate circularly-polarized THz wave emission from a
281 laser wake-field formed in front of the water flow. Further control of THz wave polarization,
282 from linear to circular and from left-handed to right-handed, can be well performed by adjusting
283 such spatial offsets and time delay. With the appropriate offsets, THz emission intensity is also
284 enhanced 1,500-times if it is compared with the single pulse irradiation. This corresponds to
285 the photon-number-based conversion efficiency from the laser to THz wave under the double
286 pulse irradiation at 7.1×10^{-3} . It has a length of approximately Rayleigh length of optical focus
287 $60 \mu\text{m}$ or a sub-wavelength for the THz emission. The mechanism responsible for the increased
288 efficiency of THz wave emission as compared with the single pulse irradiation of solid/liquid/gas
289 targets is related to mass transport of ablated material/plume by the pre-pulse into the focal
290 volume of the main pulse. The strong shockwave front makes the region of the highest efficient
291 THz emission when it enters the optical path of the main pulse. It realises mass/charge delivery
292 from the side into the laser wake-field. The water ablation condition for THz wave emission is
293 optimal at the delay time of 4.7 ns after the pre-pulse irradiation when a horizontal offset between
294 the pulses was approximately diameter of the focal spot (the strongest plasma density gradient is
295 formed). Theoretically-predicted emission of circularly-polarised THz wave, when the electron
296 wake-field velocity is coupled (a cross product) with the electron density gradient, is realised
297 experimentally in this study. The radial current transients restoring the axially depleted charges in
298 the wake-field determines the spectral extent (a shorter transient broader spectrum as related via
299 Fourier transform) and the circular polarisation of such THz wave emission. Circular polarisation
300 is a result of radially-spiraling currents. for Circularly-polarised THz wave emission opens
301 new possibilities as a polarisation control toolbox for THz technologies which can open new
302 applications for opto-mechanics where large torsion can be generated upon absorption, reflection,
303 or scattering and for rotational/vibrational molecular spectroscopy where polarisation wave-plates
304 are not readily available or lossy. THz wave can be used to better understand highly dynamic laser

305 triggered explosions which find increasing number of application in laser machining/fabrication
306 and creation of high temperature/pressure phases of new materials. Among different methods
307 of electromagnetic field generation, sub-wavelength emitters are promising due to unmatched
308 flexibility in wave front and polarisation engineering. THz radiation can be used to characterised
309 internal wake-field current structures in the filaments.

310 References

- 311 1. J. A. Fülöp, S. Tzortzakis, and T. Kampfrath, "Laser-driven strong-field terahertz sources," *Adv. Opt. Mater.* **8**,
312 1900681 (2020).
- 313 2. I. Dey, K. Jana, V. Y. Fedorov, A. D. Koulouklidis, A. Mondal, M. Shaikh, D. Sarkar, A. D. Lad, S. Tzortzakis,
314 A. Couairon, and G. R. Kumar, "Highly efficient broadband terahertz generation from ultrashort laser filamentation
315 in liquids," *Nat. Commun.* **8**, 1184 (2017).
- 316 3. J. Qi, E. Yiwen, K. Williams, J. Dai, and X.-C. Zhang, "Observation of broadband terahertz wave generation from
317 liquid water," *Appl. Phys. Lett.* **111**, 071103 (2017).
- 318 4. L.-L. Zhang, W.-M. Wang, T. Wu, S.-J. Feng, K. Kang, C.-L. Zhang, Y. Zhang, Y.-T. Li, Z.-M. Sheng, and X.-C.
319 Zhang, "Strong Terahertz Radiation from a Liquid-Water Line," *Phys. Rev. Appl.* **12**, 014005 (2019). Publisher:
320 American Physical Society.
- 321 5. A. V. Balakin, J.-L. Coutaz, V. A. Makarov, I. A. Kotelnikov, Y. Peng, P. M. Solyankin, Y. Zhu, and A. P. Shkurinov,
322 "Terahertz wave generation from liquid nitrogen," *Photonics Res.* **7**, 678–686 (2019). Publisher: OSA.
- 323 6. E. A. Ponomareva, A. O. Ismagilov, S. E. Putilin, A. N. Tsyarkin, S. A. Kozlov, and X. C. Zhang, "Varying pre-plasma
324 properties to boost terahertz wave generation in liquids," *Commun. Phys.* **4** (2021). Publisher: Nature Research.
- 325 7. H.-H. Huang, T. Nagashima, W.-H. Hsu, S. Juodkazis, and K. Hatanaka, "Dual THz wave and X-ray generation from a
326 water film under femtosecond laser excitation," *Nanomaterials* **8**, 523 (2018).
- 327 8. H.-H. Huang, T. Nagashima, T. Yonezawa, Y. Matsuo, S. H. Ng, S. Juodkazis, and K. Hatanaka, "Giant enhancement
328 of thz wave emission under double-pulse excitation of thin water flow," *Appl. Sci.* **10**, 2031 (2020).
- 329 9. S. Kalmykov, A. Englesbe, J. Elle, and A. Schmitt-Sody, "Single-cycle thz signal accompanying laser wake in
330 photoionized plasmas," *Plasma Phys. Control. Fusion* **62**, 045008 (2020).
- 331 10. A. Kramida, Yu. Ralchenko, J. Reader, and NIST ASD Team, NIST Atomic Spectra Database (ver. 5.8),
332 [Online]. Available: <https://physics.nist.gov/asd> [2021, June 30]. National Institute of Standards and
333 Technology, Gaithersburg, MD. (2020).
- 334 11. W. M. Wood, C. W. Siders, and M. C. Downer, "Femtosecond Growth Dynamics of an Underdense Ionization Front
335 Measured by Spectral Blueshifting," *IEEE TRANSACTIONS ON PLASMA SCIENCE* **21**, 14 (1993).
- 336 12. B. M. Penetrante, W. M. Wood, C. W. Siders, J. N. Bardsley, and M. C. Downer, "Ionization-induced frequency shifts
337 in intense femtosecond laser pulses," *J. Opt. Soc. Am. B* **9**, 2032 (1992).
- 338 13. K. Hatanaka, T. Miura, and H. Fukumura, "Ultrafast x-ray pulse generation by focusing femtosecond infrared laser
339 pulses onto aqueous solutions of alkali metal chloride," *Appl. Phys. Lett.* **80**, 3925–3927 (2002).
- 340 14. F. Blanchard, L. Razzari, H.-C. Bandulet, G. Sharma, R. Morandotti, J.-C. Kieffer, T. Ozaki, M. Reid, H. F. Tiedje,
341 H. K. Haugen, and F. A. Hegmann, "Generation of 1.5 μ J single-cycle terahertz pulses by optical rectification from a
342 large aperture ZnTe crystal," *Opt. Express* **15**, 13212–13220 (2007). Publisher: OSA.
- 343 15. H.-H. Huang, S. Juodkazis, E. G. Gamaly, T. Nagashima, T. Yonezawa, and K. Hatanaka, "THz wave emission from
344 air under femtosecond double pulse with nanosecond time-delay and micrometer spatial-offsets," under preparation
345 (2021).
- 346 16. K. Mori, M. Hashida, T. Nagashima, D. Li, K. Teramoto, Y. Nakamiya, S. Inoue, and S. Sakabe, "Directional linearly
347 polarized terahertz emission from argon clusters irradiated by noncollinear double-pulse beams," *Appl. Phys. Lett.*
348 **111**, 241107 (2017).
- 349 17. J. Zhou, X. Rao, X. Liu, T. Li, L. Zhou, Y. Zheng, and Z. Zhu, "Temperature dependent optical and dielectric
350 properties of liquid water studied by terahertz time-domain spectroscopy," *AIP Adv.* **9**, 035346 (2019).
- 351 18. S. Kalmykov, A. Englesbe, J. Elle, and A. Schmitt-Sody, "Single-cycle thz signal accompanying laser wake in
352 photoionized plasmas and plasma channels," *J Physics: Confer. Ser.* **1596**, 012060 (2020).
- 353 19. S. Kalmykov, J. Elle, and A. Schmitt-Sody, "Radiation emission at Langmuir frequency from laser wake in
354 longitudinally stratified plasma column," *Plasma Phys. Control. Fusion* **62**, 115022 (2020).
- 355 20. G. L. Dakovski, B. Kubera, and J. Shan, "Localized terahertz generation via optical rectification in znTe," *J. Opt. Soc.*
356 *Am. B* **22**, 1667–1670 (2005).
- 357 21. F. C. P. Masim, M. Porta, W.-H. Hsu, M. T. Nguyen, T. Yonezawa, A. Balčytis, S. Juodkazis, and K. Hatanaka, "Au
358 nanoplasma as efficient hard X-ray emission source," *ACS Photonics* **3**, 2184 – 2190 (2016).
- 359 22. H.-H. Huang, Y.-t. R. Chau, T. Yonezawa, M. T. Nguyen, S. Zhu, D. Deng, T. Nagashima, and K. Hatanaka, "THz
360 wave emission from znTe nano-colloidal aqueous dispersion irradiated by femtosecond laser," *Chem. Lett.* **49**, 597–600
361 (2020).
- 362 23. D. Attwood, *Soft X-Rays and Extreme Ultraviolet Radiation: Principles and Applications* (Cambridge University
363 Press, Cambridge, 1999).
- 364 24. K. Hatanaka, T. Ida, H. Ono, S.-i. Matsushima, H. Fukumura, S. Juodkazis, W. Siders, A. Cavalleri, K. Sokolowski-
365 Tinten, C. Toth, T. Guo, M. Kammler, M. H. v. Hoegen, K. R. Wilson, D. v. d. Linde, C. P. J. Barty, F. Girard,

- 366 O. Peyrusse, and J.-c. Gauthier, "Chirp effect in hard X-ray generation from liquid target when irradiated by
367 femtosecond pulses," *Science* **70**, 1340 (1997).
- 368 25. P. Yeh, "A new optical model for wire grid polarizers," *Opt. Commun.* **26**, 289 – 292 (1978).
- 369 26. F. Miyamaru, T. Kondo, T. Nagashima, and M. Hangyo, "Large polarization change in two-dimensional metallic
370 photonic crystals in subterahertz region," *Appl. Phys. Lett.* **82**, 2568–2570 (2003).
- 371 27. N. Kanda, K. Konishi, and M. Kuwata-Gonokami, "Terahertz wave polarization rotation with double layered metal
372 grating of complimentary chiral patterns," *Opt. Express* **15**, 11117–11125 (2007).

373 5. Experiments

374 All the experiments shown in Fig.10 were carried out in air under atmospheric pressure (1 atm)
375 at room temperature (296 K).

376 **Polarization-sensitive THz time-domain spectroscopy.** The setup is as shown in Fig.10 (a). A
377 pulsed femtosecond laser ($t_p = 35$ fs, transform-limited, $\lambda = 800$ nm, 1 kHz, Mantis, Legend
378 Elite HE USP, Coherent, Inc.,) is used and the output pulses are split into the pre-pulse (E_1 ,
379 linearly-polarized parallel to y-axis, y-pol., 0.2 mJ/pulse), the main pulse (E_2 , linearly-polarized
380 parallel to x-axis, x-pol., 0.4 mJ/pulse), and the probe for THz time-domain spectroscopy (TDS)
381 with a series of half-wave plates and polarization beam splitters (65-906, 47-048, Edmund
382 Optics) [7, 8, 22]. THz wave emission is induced by the main pulse irradiation with time-delay,
383 Δt , to the pre-pulse irradiation onto a thin water flow (~ 17 μm thick) by an off-axis parabolic
384 mirror (1-inch diameter, effective focal length $f = 50.8$ mm, 47-097, Edmund Optics). The laser
385 incident angle along z-axis is at 60° to the water surface normal. With this incident angle at 60° ,
386 effective coupling between the incident laser and the self-generating plasma is highly expected
387 thorough resonance absorption [23], which has been confirmed in hard X-ray generation from
388 water [24]. Under this condition, the polarisations of the main and the pre-pulses are p-pol. and
389 s-pol., respectively. The optical delay between the two excitation pulses, Δt , is controlled with
390 automatic stages (SGSP46-800 and SGSP26-150, Sigma Koki). A water flow is prepared with
391 two colliding water jets and the system is set on an automatic stage (KS701-20LMS, Suruga
392 Seiki) along the z-axis to adjust the flow surface for optimal X-ray emission measured by a Geiger
393 counter (SS315, Southern Scientific). The detection of the THz wave emission is carried out by
394 the electro-optic sampling method in the transmission direction through the water flow and in the
395 reflection direction with $\langle 110 \rangle$ -oriented ZnTe crystals (1-mm thick, Nippon Mining & Metals
396 Co., Ltd.). Lock-in measurements are carried out with an optical chopper (3502, New Focus)
397 and a lock-in amplifier (SR830, Stanford Research System), therefore the effective repetition
398 rate of the laser excitation is 0.5 kHz. Following the usual method reported previously [25–27],
399 two wire grids (WGs, MWG40FA-III, Origin) are additionally used for the measurements of
400 polarization status in THz wave emission. One of the WGs, WG2, is used at the fixed angle
401 0° (parallel to x-axis), while the other WG, WG1, is used at two different angles, $+45^\circ$ and -45° for
402 two independent TDS signals as E_{+45} and E_{-45} , respectively. The x- and y-components of THz
403 electric field, E_x and E_y , are then calculated from $E_x = E_{+45} + E_{-45}$ and $E_y = E_{+45} - E_{-45}$,
404 respectively.

405 **Time-resolved imaging.** Imaging experiments for the laser focus from the side (along x-axis)
406 and the top (6° -tilted from y-axis) are as shown in Fig.10 (b) and carried out in two different
407 methods with an objective lens (M Plan Apo 10 \times , or M Plan UV 10 \times , MITUTOYO) and CMOS
408 cameras (Blackfly S USB3, FLIR Systems, Inc.) with filters for IR-cut and for intensity control
409 in the visible region. One is with the pre-pulse and white light continuum (~ 1 ps, 580 ± 30 nm,
410 as a strobe light) converted from the main pulse with a water cell. With this method, transient
411 refractive index changes and/or scattering due to pre-plasma formation and/or laser ablation
412 induced by the pre-pulse irradiation can be visualized. Another imaging is with the pre-pulse
413 and the main pulse, which visualizes the interaction of the main pulse with the water flow with
414 structures prepared by the pre-pulse irradiation. The exposure time for the camera setting was
415 fixed at 2 ms for single shot imaging. In this mode of image acquisition, all the emission in

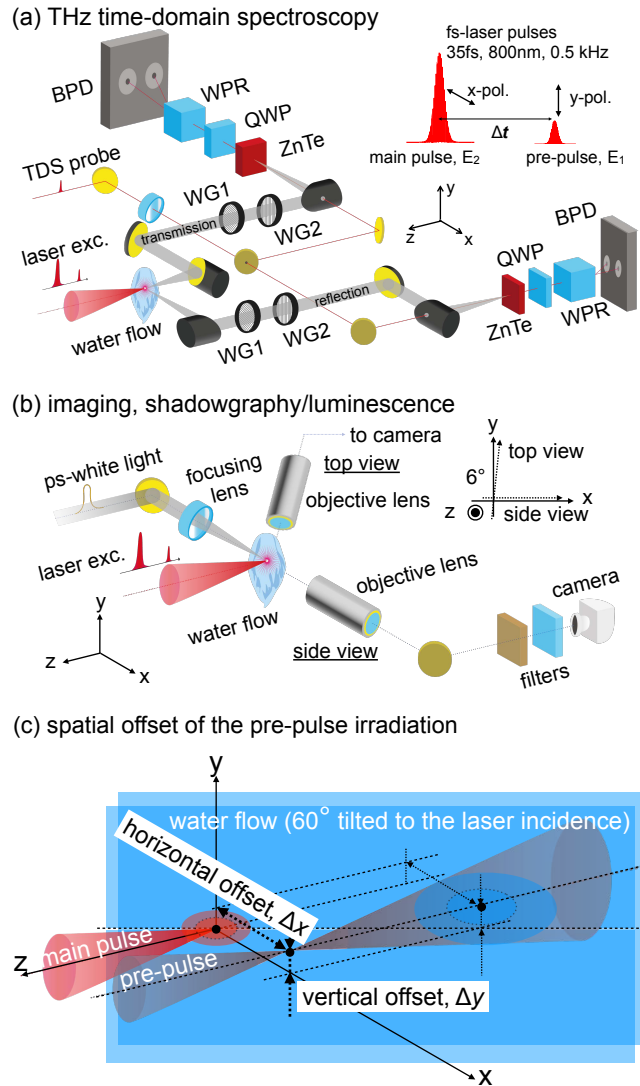


Fig. 10. The experimental setups for THz time-domain spectroscopy (TDS) for the transmission and the reflections sides (a) and time-resolved shadowgraphy under the pre-pulse irradiation with picosecond white-light back illumination and time-integrated luminescence images under the single (only with the main pulse) and the double pulse excitation condition (b). A schematic diagram for the horizontal and vertical offsets, Δx and Δy , for the pre-pulse irradiation (c).

416 broad-band spectra by the two-pulse irradiation of the water flow is time-integrated. In associated
 417 with the imaging, time-integrated UV-visible emission spectroscopy is also performed with a
 418 commercially-available spectrometer (HR4000, OceanInsight), which is position-dependent with
 419 a fiber-input.

420 **Pre-pulse spatial offsets.** In addition to the time-delay as the temporal offset, spatial offsets
 421 along x- and y-axes, Δx and Δy , are applied to the pre-pulse irradiation in the experiments
 422 described above as shown in Fig.10 (c). One steering mirror for the pre-pulse alignment is
 423 automatically controlled by a piezo-transducer system (POLARIS-K2S2P, KPZ101, Thorlabs) to

424 change the pre-pulse focus position with micron-order precision. The origin, $(\Delta x, \Delta y) = (0, 0)$, is
425 defined experimentally with a Newton-ring like pattern in far field to the transmission side as an
426 interference pattern with the pre-pulse and the main pulse focuses in air. The focus position of
427 the pre-pulse with offsets is experimentally confirmed by the imaging setup described above.

428 **Disclosures.** The authors declare no conflicts of interest.

429 **Data Availability Statement.** Data underlying the results presented in this paper are not publicly available
430 at this time but may be obtained from the authors upon reasonable request.

Supplementary Files

This is a list of supplementary files associated with this preprint. Click to download.

- [commsphys2022supplimentdoubleblind.pdf](#)